Research Square

Preprints are preliminary reports that have not undergone peer review.
They should not be considered conclusive, used to inform clinical practice,
or referenced by the media as validated information.

Polymer-supported cryo-FIB milling enables near-native structural analysis of mature bacterial spores

Tasuku Hamaguchi

tasuku.hamaguchi.c3@tohoku.ac.jp

IMRAM, Tohoku University https://orcid.org/0000-0003-0876-7700

Rumi Niwa

IMRAM, Tohoku University

Takuma Toyonaga

IMRAM, Tohoku University

Keisuke Kawakami

RIKEN https://orcid.org/0000-0002-1689-1819

Daisuke Unabara

Tohoku University https://orcid.org/0000-0001-5347-7257

Koji Yonekura

RIKEN SPring-8 Center https://orcid.org/0000-0001-5520-4391

Article

Keywords:

Posted Date: November 11th, 2026

DOI: https://doi.org/10.21203/rs.3.rs-11562310/v1

License: This work is licensed under a Creative Commons Attribution 4.0 International License.
Read Full License

Additional Declarations: There is **NO** Competing Interest.

Polymer-supported cryo-FIB milling enables near-native structural analysis of mature bacterial spores

Rumi Niwa[1,†], Takuma Toyonaga[2,†], Keisuke Kawakami[3], Daisuke Unabara[2,4], Koji Yonekura[1,2,3,4,*], Tasuku Hamaguchi[1,2,4,*]

[1] Graduate School of Life Sciences, Tohoku University. Katahira 2-1-1, Aoba-ku, Sendai, Miyagi, Japan

[2] Institute of Multidisciplinary Research for Advanced Materials, Tohoku University. Katahira 2-1-1, Aoba-ku, Sendai, Miyagi, Japan

[3] Biostructural Mechanism Laboratory, RIKEN SPring-8 Center. Kouto 1-1-1. Sayo, Hyogo, Japan

[4] Tohoku Center of Excellence for Microscopy, Tohoku University. Katahira 2-1-1, Aoba-ku, Sendai, Miyagi, Japan

[†] These authors contributed equally.

* Corresponding Authors, Tasuku Hamaguchi (tasuku.hamaguchi.c3@tohoku.ac.jp) and Koji Yonekura (koji.yonekura.a5@tohoku.ac.jp; yone@spring8.or.jp).

Abstract

Bacterial spores exhibit remarkable resistance to environmental stresses, posing challenges for food safety and sterilization. In *Bacillus subtilis* var. *natto*, spores are embedded within a viscous extracellular matrix rich in γ-polyglutamic acid (γ-PGA), yet their internal membrane architecture and spatial relationships with the surrounding matrix remain poorly understood. Here, we develop polymer-supported cryogenic focused ion beam (PolyS-FIB) milling and combine it with cryogenic transmission electron microscopy (cryo-TEM) and cryo-electron tomography (cryo-ET) to investigate mature spores under near-native conditions. The polymer support improves sample adhesion and lamella stability, enabling two- and three-dimensional visualization of spores embedded within the extracellular matrix. We identify morphologically diverse sub-core membranes (SCMs), including single- and double-layered configurations, complex membrane structures associated with invaginations of the inner membrane (IM), together with vesicle-like structures within these regions. Quantitative analysis reveals a significant difference in apparent membrane thickness between the IM and the inner layer of double-layered SCMs. Three-dimensional imaging further resolves the multilayered spore coat and membrane-like structures at the spore periphery, while complementary cryo-ultramicrotomy reveals spatial heterogeneity in the surrounding extracellular matrix. Together, these findings provide new insights into the membrane architecture of mature bacterial spores and establish PolyS-FIB as a sample preparation strategy for investigating

biological structures embedded within complex extracellular environments.

Introduction

Bacterial spores represent one of the most resistant forms of life, enabling long-term survival under extreme environmental conditions, including heat, desiccation, radiation, and chemical stress[1]. This remarkable resilience is a defining feature of many spore-forming bacteria, such as *Bacillus* and *Clostridium* species, which are of major relevance to food safety, environmental microbiology, and infectious disease[2]. Despite extensive studies on spore structure, the detailed organization of internal membrane structures in mature spores and their structural relationship with surrounding extracellular environments remain incompletely understood.

Natto, a traditional Japanese fermented soybean product produced by *Bacillus subtilis* var. *natto*, provides a unique model system for investigating spores embedded within a dense extracellular matrix. During fermentation, the bacterium secretes γ-polyglutamic acid (γ-PGA), a highly hydrated polymer that forms a viscous matrix surrounding cells and spores[3,4]. While γ-PGA has been widely studied for its physicochemical and industrial properties[5], its structural role in organizing and stabilizing spores *in situ* has not been elucidated. More broadly, extracellular polymeric matrices are increasingly recognized as key components of microbial survival strategies, yet their spatial organization relative to dormant cells remains poorly characterized[6,7].

Current understanding of spore architecture has largely been derived from transmission electron microscopy (TEM) studies of chemically fixed and sectioned samples[8,9]. These approaches have established the multilayered organization of spores, including the core, inner membrane, cortex, coat, and outer layers[10–12]. However, the three-dimensional organization of internal membrane structures including sub-core membranes (SCMs), and their relationships with the inner membrane remain poorly characterized. Moreover, conventional preparation methods can introduce structural artifacts, potentially affecting the preservation of delicate membrane architectures. Cryogenic transmission electron microscopy (cryo-TEM) enables visualization of biological specimens in a near-native, hydrated state without chemical fixation or staining[13]. When combined with cryogenic focused ion beam (cryo-FIB) milling and cryo-electron tomography (cryo-ET), this approach provides access to the internal three-dimensional architecture of thick biological specimens[14]. However, preparing stable, electron-transparent lamellae from specimens embedded within dense extracellular polymer networks remains technically challenging, particularly because of insufficient sample adhesion and mechanical instability during cryo-FIB milling.

Here, we introduce polymer-supported cryo-FIB (PolyS-FIB) milling, a sample preparation strategy designed to improve sample adhesion and lamella stability during cryogenic thinning. By integrating PolyS-FIB with cryo-TEM and cryo-ET, we enable near-native two- and three-dimensional structural analysis of mature spores of *Bacillus subtilis* var. *natto* embedded within extracellular

polymer networks[15] (Fig. 1). This approach reveals the morphological diversity and heterogeneous three-dimensional distribution of SCMs, including single-layered and double-layered configurations with a preferential localization near the core periphery. We further identify complex membrane invaginations and associated vesicle-like structures, providing a structural basis for proposing hypothetical pathways of SCM formation. In addition, we characterize the multilayered spore envelope and the surrounding extracellular matrix. Together, these findings demonstrate the utility of PolyS-FIB for investigating delicate membrane architectures in complex biological environments and provide new insights into the structural organization of mature bacterial spores under near-native conditions.

Results

Visualization of *Bacillus subtilis* cells in natto

Light microscopy observations revealed that natto filaments contain abundant vegetative cells and spores (Supplementary Fig. 1, Supplementary Movie 1). Consistent with these observations, cryo-TEM imaging of the filament suspension also showed both vegetative cells and spores. However, due to the substantial thickness of the cells, internal structural details could not be clearly resolved, indicating the need for sample thinning for high-resolution analysis (Supplementary Fig. 2).

Development and optimization of polymer-supported cryo-FIB (PolyS-FIB) milling

Prior to polymer coating, natto filaments were directly applied onto EM grids with a holey carbon film, vitrified, and examined by cryo-scanning electron microscopy (SEM) with FIB. Under these conditions, the filaments frequently appeared partially detached from the grid surface, reflecting low affinity to the carbon support film (Supplementary Fig. 3a). This poor adhesion led to failures in eucentric alignment during automated FIB milling. In addition, the absence of a solvent layer on the carbon support reduced mechanical stability, resulting in deformation or breakage during stress-relief cutting and milling (Supplementary Fig. 3b). Consequently, most of the resulting lamellae were unsuitable for subsequent cryo-TEM observation. To overcome these limitations, we developed a polymer-supported cryo-focused ion beam milling strategy, termed PolyS-FIB, in which a thin polymer film is introduced onto carbon support to improve sample adhesion and mechanical stability during cryo-FIB processing (Fig. 1).

The natto filaments were subsequently deposited onto polymer-coated grids and subjected to cryo-TEM observation. Cryo-TEM observations at a nominal magnification of 150× showed that the application of 0.5% (w/w) γ-PGA, followed by blotting with filter paper, resulted in the formation of a thin film that was sufficiently electron-transparent (Supplementary Fig. 4a). In contrast, although a film was also formed using 2.0% (w/w) γ-PGA, the transmitted electron intensity was substantially reduced, indicating that the resulting film was too thick for cryo-TEM imaging (Supplementary Fig.

4b). Low-magnification observations of grids with attached natto filaments demonstrated that, under both γ-PGA and poly(acrylic acid) (PAA) coating conditions, the filaments adhered well to each support film while maintaining their original morphology (Supplementary Fig. 5a,c). The filament edges were observed to spread along the film surface, forming flattened structures. Within these regions, multiple cellular features consistent with vegetative cells and spores were observed, indicating that bacterial cells were distributed within the filaments (Supplementary Fig. 5b,d). The resistance of the polymer films to electron beam irradiation was further evaluated. In PAA-coated grids, the appearance of fine bubbles across the imaging area was observed at a cumulative electron dose of 59.4 $e^{-}/Å^{2}$, and the bubble area increased with continued irradiation (Fig. 2). In contrast, in γ-PGA-coated grids, only minor damage was observed at the hole edges at a dose of 79.2 $e^{-}/Å^{2}$. Upon further irradiation up to a total dose of 115.4 $e^{-}/Å^{2}$, damage remained localized near the hole edges, and no widespread bubble formation across the film was observed. Based on these observations, γ-PGA was selected as the support material for PolyS-FIB milling and subsequent cryo-TEM analyses.

Imaging results of spores in lamellae

Compared with preparation without polymer support, PolyS-FIB milling yielded lamellae with fewer observable cracks and curtaining artifacts, facilitating subsequent cryo-TEM imaging

(Supplementary Table 1). Cryo-TEM imaging of the resulting lamellae revealed the internal architecture of mature spores embedded within the extracellular matrix (Fig. 3b and Supplementary Fig. 6). The spores exhibited heterogeneous morphologies while retaining their characteristic multilayered organization, including the core, inner membrane (IM), cortex, inner coat (IC), and outer coat (OC) (Figs. 3c, 4). The IM was clearly resolved as a lipid bilayer surrounding the core. The IC exhibited a periodic lamellar organization, typically consisting of three to four repeating units, whereas the OC showed a more heterogeneous structure (Fig. 4e,f). In addition, membrane-like structures were observed at the outermost boundary of some spores, potentially representing remnants of the mother cell-derived outer forespore membrane (Fig. 4g). Within the spore core, distinct membrane-like structures, referred to as sub-core membranes (SCMs), were observed (Fig. 4b-d and Supplementary Fig. 6). These structures exhibited considerable morphological diversity, including curved membrane configurations associated with inward invagination of the IM, partially double-layered structures, and double-layered structures appearing spatially separated from the IM. A vesicle-like structure was also observed near an invaginated region of the IM (Fig. 4b). These two-dimensional observations revealed the structural heterogeneity of SCMs and suggested a possible spatial relationship between SCMs and the IM.

To investigate the three-dimensional organization of SCMs, we performed cryo-electron tomography (cryo-ET) on mature spores prepared using PolyS-FIB milling (Fig. 5, Supplementary Movies 2 and

3). A zero-degree tilt projection image provided an overview of the spore architecture (Fig. 5a), while tomographic slices at different depths revealed variations in the morphology and spatial distribution of SCMs within the same spore (Fig. 5b–d, Supplementary Movies 4 and 5). Three-dimensional segmentation and rendering further distinguished single-layered and double-layered SCM configurations and revealed their distribution relative to the surrounding IM (Fig. 5e, Supplementary Movie 6). SCMs were observed at multiple locations throughout the peripheral region of the spore core, predominantly near the IM, whereas relatively few SCMs were detected in the central region. These observations indicate that SCMs exhibit a heterogeneous spatial distribution within individual mature spores, with a preferential localization near the core periphery. During tilt-series acquisition, bubble-like features appeared in the extracellular matrix at high tilt angles, consistent with radiation-induced damage associated with the accumulated electron dose. Further examination of reconstructed tomograms revealed complex membrane architectures associated with inward invaginations of the IM (Fig. 6a–d, Supplementary Movies 5 and 7). In these regions, the invaginated membranes exhibited pronounced curvature and irregular folding and remained connected to the surrounding IM at multiple sites. These interconnected membrane regions also contained features suggestive of vesicle-like structures, highlighted in cyan in Fig. 6b–d (Supplementary Movies 7 and 8). Tomographic slices at different depths revealed variations in the appearance of these membrane structures, providing additional information about their three-

dimensional organization. These observations suggest a spatial relationship between IM invagination, vesicle-like structures, and SCM organization, although the sequence of membrane remodeling events and the formation pathway of SCMs cannot be determined from static tomographic observations. In contrast, SCMs located away from the IM exhibited either single-layered or double-layered configurations, without detectable vesicle-like structures (Fig. 6e). In addition, regions exhibiting distinct image contrast and bounded by membrane-like structures were observed outside the OC. These features may be associated with the spore crust or represent remnants of the outer forespore membrane, although their molecular identity remains uncertain (Fig. 6f,g).

The multilayered organization of the IC was also resolved in the reconstructed tomograms. To examine structural differences between SCMs and the IM, membrane thicknesses were quantitatively compared using reconstructed tomographic sections (Supplementary Fig. 7a,b). Measurements were obtained from five spores, with ten measurements per membrane group in each spore. The IM exhibited the greatest mean thickness (7.00 ± 0.29 nm), followed by the outer layer of double-layered SCMs (6.48 ± 0.23 nm), single-layered SCMs (6.45 ± 0.41 nm), and the inner layer of double-layered SCMs (6.15 ± 0.26 nm; mean ± SD, n = 5 spores per group). Repeated-measures ANOVA revealed a significant effect of membrane type on thickness (Greenhouse–Geisser-corrected $P = 0.041$) (Supplementary Fig. 7c). Tukey-adjusted pairwise comparisons showed that the IM was

significantly thicker than the inner layer of double-layered SCMs (mean difference, 0.84 nm; $P = 0.0066$), whereas no other pairwise comparisons were statistically significant ($P > 0.05$). A linear mixed-effects model accounting for measurements clustered within each spore–membrane group also revealed a significant effect of membrane type ($P = 0.0042$), with a significant difference between the IM and the inner layer of double-layered SCMs (Tukey-adjusted $P = 0.0025$). In contrast, a simpler linear mixed-effects model including only spore identity as a random intercept identified significant differences between the IM and all three SCM membrane groups (Tukey-adjusted $P < 0.05$). However, the additional differences involving the outer layer of double-layered SCMs and single-layered SCMs were not statistically significant in the model accounting for clustering within spore–membrane groups. Thus, the greater apparent thickness of the IM relative to the inner layer of double-layered SCMs was consistently supported across all three statistical approaches. The number of SCMs also varied substantially among individual spores, with no clear correlation with core area (Supplementary Table 2).

Extracellular matrix surrounding spores

We also prepared thin sections by cryo-ultramicrotomy to examine the extracellular matrix surrounding spores over large areas. In samples prepared by slow freezing in liquid nitrogen, low-magnification images of the sections revealed the presence of cracks aligned parallel to the cutting

direction of the diamond knife, along with pronounced wrinkles oriented perpendicular to the cutting direction (Fig. 7a). As a result, the regions suitable for observation were limited. At a higher magnification, two distinct regions with different contrast were observed in the vicinity of spores (enclosed by solid and dashed boxes in Fig. 7b). One region (solid box) exhibited lower contrast and showed partially crystalline features, whereas the other region (dotted box) exhibited higher contrast and remained amorphous, as confirmed by their Fourier transforms (Fig. 7c, d). These two regions were spatially separated within the section. Layered structures were observed in the region enclosed by the two arrowheads at the periphery of the spores. However, the contrast between individual layers was weak, preventing detailed characterization of the respective layers, and no clear structural details were obtained from the core region. In samples prepared by rapid freezing in liquid ethane, low-magnification images showed a mesh-like distribution of contrast across the sections (Fig. 7e, f). Regions corresponding to the low-contrast areas observed in liquid nitrogen-frozen samples were absent and appeared as holes within the sections. This observation is likely attributable to differences in mechanical properties between the two regions at the sectioning temperature, resulting in non-uniform cutting during cryo-ultramicrotomy. Consequently, regions that appeared crystalline in the slowly frozen samples may have been preferentially removed during sectioning, leaving voids in the ultrathin sections. At higher magnification, tearing of the sections was observed along the boundaries between spores and the surrounding matrix (Fig. 7g). In addition, spore structures exhibited

deformation consistent with compression along the cutting direction. Taken together, these observations demonstrate that cryo-ultramicrotomy enables large-scale visualization of the extracellular environment and reveals heterogeneous distributions of matrix components surrounding spores. However, differences in the mechanical properties of the matrix appear to result in non-uniform sectioning, leading to local loss of structural information during section preparation. In contrast, cryo-FIB lamellae preserve a more continuous and hydrated matrix architecture, supporting the presence of a native polymer network while maintaining local structural integrity.

Discussion

This study establishes polymer-supported cryo-FIB (PolyS-FIB) milling as a sample preparation strategy for structural analysis of biological specimens embedded within complex extracellular polymer networks. Conventional cryo-FIB milling can be challenging for such specimens because insufficient adhesion to support grids and mechanical instability during thinning may lead to sample deformation, cracking, or lamella failure. By introducing a thin polymer film onto holey carbon grids, PolyS-FIB provides additional mechanical support and improves specimen attachment during cryogenic milling. In the present study, γ-PGA was selected as the support material based on its ability to form an electron-transparent film, support natto filaments, and withstand electron irradiation with limited observable damage. This approach facilitated the preparation of cryo-FIB

lamellae suitable for cryo-TEM and cryo-ET, enabling detailed two- and three-dimensional characterization of mature *Bacillus subtilis* var. *natto* spores within their extracellular matrix. The resulting observations reveal previously less-characterized internal membrane architectures, demonstrating how improvements in cryogenic sample preparation can provide access to biological structures that are difficult to investigate using conventional approaches[13].

One of the most notable findings was the morphological diversity and heterogeneous three-dimensional distribution of SCMs. Two-dimensional cryo-TEM observations revealed curved, partially double-layered, and double-layered SCM configurations, including membrane structures associated with inward invaginations of the IM. Three-dimensional segmentation further revealed that single-layered and double-layered SCMs were distributed at multiple locations within the spore core, predominantly near the IM, whereas relatively few SCMs were observed in the central region. This peripheral distribution suggests a possible structural relationship between SCM organization and the surrounding IM. Furthermore, reconstructed tomograms revealed complex membrane invaginations containing vesicle-like structures, suggesting that membrane remodeling and vesicle formation may be associated with SCM organization. In contrast, SCMs located away from the IM exhibited single-layered or double-layered configurations without detectable vesicle-like structures. This morphological difference may reflect distinct stages of membrane remodeling or structural maturation, although the temporal relationship between these configurations remains unclear.

Previous cryo-electron tomography studies have revealed extensive membrane remodeling during *Bacillus subtilis* sporulation, providing a structural context for considering the possible origin of SCMs. However, whether the membrane configurations observed in mature spores arise through related processes remains unknown[15] .

Based on these observations, we propose two hypothetical pathways for the formation of double-layered SCMs involving invagination and fusion of the IM (Fig. 8). In the single-invagination fusion model, an inward invagination of the IM expands laterally and subsequently fuses with the surrounding IM, generating an internal membrane vesicle. In the multiple-invagination fusion model, adjacent invaginations of the IM fuse with one another, resulting in the formation of internal vesicles. In both models, the internal vesicles may subsequently fuse to form the inner SCM, while the surrounding invaginated IM forms the outer SCM, resulting in a double-layered SCM configuration. These models provide possible explanations for the coexistence of single-layered, double-layered, and vesicle-associated membrane structures observed within mature spores. However, the proposed membrane fusion events and the temporal sequence of SCM formation have not been directly demonstrated. Because cryo-ET provides static structural information, the models remain hypothetical, and further investigations of spores at different stages of maturation will be required to clarify the origin and formation mechanisms of SCMs.

Quantitative analysis of membrane thickness revealed a significant difference between the IM and

the inner layer of double-layered SCMs. This difference was consistently supported by repeated-measures ANOVA and a linear mixed-effects model accounting for measurements clustered within individual spore–membrane groups. A simpler mixed-effects model including only spore identity as a random intercept also identified significant differences between the IM and the other two SCM membrane groups. However, these additional differences were no longer statistically significant when variability among membrane groups within individual spores was taken into account. This sensitivity to model specification highlights the need for caution in interpreting small differences in membrane thickness, particularly given the limited number of spores examined.

The observed difference in apparent membrane thickness may be associated with differences in membrane organization or local structural environments, although its molecular basis remains unknown. Importantly, the measured membrane thicknesses (approximately 6–7 nm) should be interpreted as apparent rather than absolute values. Measurements were based on the distance between contrast minima in reconstructed tomographic sections, which may not directly correspond to the physical boundaries of the lipid bilayer. Furthermore, apparent membrane thickness in cryo-ET may be influenced by membrane orientation relative to the tomographic section, particularly when measurements are not performed perpendicular to the local membrane surface. Differences in membrane curvature between the IM and SCMs may therefore introduce systematic variations in apparent membrane thickness. Accordingly, these measurements are more appropriately interpreted

as relative estimates for comparisons among membrane groups rather than absolute measurements of lipid bilayer thickness. Despite these limitations, the detection of differences in apparent membrane thickness highlights the potential of PolyS-FIB combined with cryo-ET for quantitative characterization of internal membrane architecture *in situ*. Further development of higher-throughput approaches enabling the analysis of larger numbers of spores will be necessary to establish the reproducibility and biological significance of these differences.

Three-dimensional cryo-ET analysis also provided detailed views of the multilayered spore envelope. The inner coat exhibited a periodic lamellar organization consisting of alternating layers of different image contrast, consistent with the complex structural organization of bacterial spore coats. In addition, regions exhibiting distinct image contrast and delimited by membrane-like boundaries were observed outside the outer coat. These features suggest a more complex organization of the outermost spore layers than could be inferred from conventional two-dimensional observations. These observed structures may be associated with the spore crust or represent remnants of the outer forespore membrane. However, because the crust is generally considered a proteinaceous outer layer, the observed membrane-like boundaries cannot be assigned to either structure based on morphology alone. Further structural and molecular characterization will be required to establish their identity. The near-native preservation afforded by cryogenic preparation allowed clearer visualization of structural boundaries that may be difficult to distinguish in chemically fixed samples. This suggests

that some differences between the present observations and previous reports may arise, at least in part, from differences in sample preparation[9,11,12].

Another important aspect of this study is the spatial organization of spores within the extracellular matrix. The extracellular matrix, expected to be rich in γ-PGA, surrounds the spores and may contribute to their physical stabilization[6,7]. In addition to contributing to the characteristic viscosity of natto, the γ-PGA-rich matrix may influence the spatial organization of spores within their extracellular environment. The organization of the extracellular matrix was investigated using complementary cryo-FIB lamella imaging and cryo-ultramicrotomy, enabling visualization across multiple length scales. These approaches revealed spatially heterogeneous regions within the extracellular matrix, potentially reflecting differences in local polymer and water content. Such heterogeneity may contribute to differences in the local physical conditions experienced by individual spores, although its direct relationship to spore resistance remains to be established.

From a functional perspective, the observed structural organization raises the possibility of a multiscale protective system involving both the highly dehydrated spore core and the surrounding hydrated extracellular matrix. The internal architecture of the spore contributes to its intrinsic stability, whereas the extracellular polymer matrix may provide additional physical shielding against environmental stresses. However, the protective contribution of the matrix was not directly evaluated in this study, and further experiments will be necessary to establish its functional significance.

Understanding the relationship between spore architecture and extracellular organization may provide insights relevant to sterilization, control of spore persistence, and the development of biomimetic protective materials.

Beyond the structural insights into bacterial spores, the present study highlights the broader potential of PolyS-FIB as a sample preparation strategy for biological specimens that are difficult to support and thin using conventional cryo-FIB approaches. Once the polymer support film has been prepared, biological specimens can be directly deposited onto the grid without prior dispersion in an externally added aqueous solution. This feature may be particularly advantageous for specimens whose native organization depends on extracellular polymers, fibrous networks, or highly viscous biological matrices. Potential applications include microbial biofilms, fungal hyphal networks, bacterial cellulose-associated communities, and other biological assemblies embedded within extracellular polymeric substances. In such systems, polymer-supported preparation could facilitate the investigation of cellular structures and their spatial relationships with the surrounding matrix while minimizing disruption associated with sample dispersion or extensive manipulation. Furthermore, the choice of supporting polymer could potentially be adapted to the physicochemical properties of different specimens. Nevertheless, successful application to other biological systems will require optimization of polymer film properties, specimen attachment, vitrification conditions, and milling parameters according to the characteristics of each sample. Together, these findings position PolyS-

FIB as a promising approach for extending cryo-FIB milling and cryo-electron tomography to challenging biological specimens with complex extracellular architectures.

Materials and Methods

Light microscopy and initial cryo-TEM observations

Market natto filaments were stretched onto glass slides, covered with coverslips, and observed using phase-contrast light microscopy with an ECLIPSE Ts2R-FL microscope (Nikon) equipped with a CFI Plan Apochromat DM Lambda 100× Oil objective lens (Nikon) and an LS4MN camera (Kenis). To visualize individual bacterial cells within the extracellular matrix, natto was also suspended in phosphate-buffered saline (PBS, 137 mM NaCl, 8.1 mM Na_2HPO_4, 2.68 mM KCl, and 1.47 mM KH_2PO_4, pH 7.4), mounted on glass slides, covered with coverslips, and observed under the same imaging conditions. For initial cryo-TEM observations, filaments extended from individual natto beans at room temperature (25 °C) were attached to hydrophilized holey carbon grids (Quantifoil R2/1 Cu 200 mesh) after glow-discharge treatment (10 mA, 60 s; JEC-3000FC, JEOL). The grids were immediately transferred to an EM GP2 plunge-freezing chamber (Leica Microsystems) equilibrated at 4 °C and 95% relative humidity. To minimize drying and improve sample spreading on the grid surface, 3 μL of PBS was added to the grids. After incubation for 20 s, excess solution was removed by blotting for 3.0 s using filter paper, followed by rapid vitrification in liquid ethane

cooled to approximately −180 °C. The vitrified grids were stored in liquid nitrogen until imaging. Initial cryo-TEM observations were performed using a CRYO ARM 300 II microscope (JEOL) operated at an accelerating voltage of 300 kV and equipped with a K3 direct electron detector (Gatan, AMETEK). Images were acquired at a nominal magnification of 8,000× corresponding to a pixel size of 6.293 Å/pixel with a defocus value of −2 μm. Each exposure was recorded for 8 s, corresponding to a total electron dose of 1.56 $e^-/Å^2$, and fractionated into 50 frames for beam-induced motion correction. Inelastically scattered electrons were removed using an in-column energy filter with a 20-eV energy slit.

Polymer film preparation on support grids and electron beam stability assessment

To improve sample adhesion and support stability, polymer films were formed on holey carbon grids. γ-PGA and poly(acrylic acid) (PAA) were evaluated as support materials. Polymer solutions were prepared in Milli-Q water at concentrations of 0.5% (w/w) and 2.0% (w/w) for γ-PGA and 0.5% (w/w) for PAA. Five-μL aliquots were applied to glow-discharged grids (10 mA, 30 s), followed by gentle blotting and drying in a desiccator for at least 20 min to form thin films. Natto filaments were subsequently deposited onto the polymer-coated grids and manually vitrified, except that no PBS was added prior to vitrification. To evaluate electron beam stability, polymer-coated regions without biological material were continuously irradiated. Images were recorded at a pixel

size of 1.829 Å/pixel, and repeated exposures were applied to the same area to monitor radiation-induced damage as a function of accumulated dose.

Preparation of cryo-FIB lamellae

Grids for lamella preparation were fabricated using the γ-PGA support film selected as described above. Frozen grids were mounted onto AutoGrids under liquid nitrogen and transferred to a cryo-FIB/SEM instrument (Aquilos 2, Thermo Fisher Scientific). Prior to milling, a conductive protective layer was applied by sputter coating, followed by gas injection system (GIS) coating to enhance lamella stability and reduce curtaining artifacts[16]. An additional sputter coating step was performed to improve conductivity. Suitable regions for lamella preparation were identified by scanning electron microscopy (SEM), and milling locations were selected. Lamellae were prepared using automated milling (AutoTEM Cryo, Thermo Fisher Scientific). Based on sample geometry and eucentric alignment, milling angles of 10° and 15° were applied. Stress-relief cuts were introduced near the milling sites prior to thinning. Milling was initiated with coarse material removal and continued with progressively lower ion beam currents until the target thickness was reached, followed by final polishing steps. Additional manual polishing was subsequently performed to optimize lamella quality. The final lamella thickness was measured using xT software (Thermo Fisher Scientific) and was approximately 200–250 nm. To minimize lamella damage or delamination

and enhance conductivity, a final sputter coating (7 mA, 10 Pa, 2.0 V, 5 s) was applied. The processed grids were recovered under liquid nitrogen and stored until cryo-TEM observation.

Cryo-TEM data acquisition from lamellae

Cryo-FIB–milled grids were mounted onto AutoGrid cartridges under liquid nitrogen and transferred to the CRYO ARM 300 II. All data were acquired manually at an acceleration voltage of 300 kV using SerialEM[17,18] for microscope control in combination with Gatan Microscopy Suite (GMS, Gatan) for image recording. Images were recorded using a K3 direct electron detector (Gatan). Following low-magnification tiled imaging of the entire grid at 50× magnification, lamella regions were identified and further imaged at 150× magnification. For high-magnification imaging, the milling angle applied during cryo-FIB preparation was incorporated as the pretilt angle. Images were acquired with a defocus value of −2 µm and fractionated into 40 frames per exposure. Inelastically scattered electrons were removed using an in-column energy filter with a slit width of 20 eV. To capture both fine structural details and larger-scale organization within spores, images were recorded at magnifications of 12,000× (4.796 Å/pixel, 20.3 $e^-/Å^2$), 15,000× (3.837 Å/pixel, 30.5 $e^-/Å^2$), and 30,000× (1.829 Å/pixel, 30.2 $e^-/Å^2$), respectively.

Cryo-electron tomography data acquisition

Cryo-ET was performed to obtain three-dimensional structural information beyond two-dimensional projection images. Tilt series were acquired at 15,000× magnification (3.837 Å/pixel), with each projection image fractionated into three frames. Based on prior evaluation of radiation damage behavior, the total electron dose per tilt series was limited to 35–45 $e^{-}/Å^{2}$ by adjusting exposure times. The tilt range was determined according to the milling angle used during lamella preparation. For lamellae prepared at a milling angle of 15°, the tilt range was set from −60° to +45°, whereas for 10° milling, the range was −60° to +50°. Tilt series were acquired using a bi-directional tilt scheme with an angular increment of 5°, resulting in a total of 22 or 23 projections per tilt series using an in-house customized version of the FastTomo script[19].

Image processing, tomogram reconstruction, and three-dimensional segmentation

Tilt series were processed using RELION-5.0.0[20] and Warp-2.0.0[21,22]. Beam-induced motion correction and estimation of contrast transfer function (CTF) parameters were performed using Warp. Several high-angle tilt images were excluded from subsequent processing to improve reconstruction quality. The remaining tilt images were initially aligned using AreTomo2[23] through its wrapper implemented in RELION, followed by further refinement using Miss-alignment[24], a machine learning-based method for reference-free alignment. Tomograms were reconstructed in Warp, with reconstruction parameters adjusted according to the structures of interest, including

reconstruction thickness and CTF correction by phase flipping. Fourfold-binned tomograms (bin 4) were used for membrane segmentation and three-dimensional rendering, whereas twofold-binned tomograms (bin 2) were used for quantitative membrane thickness measurements and subsequent statistical analysis. Denoising was performed using IsoNet2[25] to improve the interpretability of the reconstructed tomograms. Non-denoised tomograms were used for segmentation of the whole-spore membrane architecture and for quantitative membrane thickness measurements, whereas IsoNet2-denoised tomograms were used for segmentation of the IM invaginations and associated vesicle-like structures shown in Fig. 6b-d. Membrane structures were segmented using Ais[26], and three-dimensional renderings of the segmented structures were generated using UCSF ChimeraX[27].

Statistical analysis

Membrane thickness was measured from five three-dimensionally reconstructed mature spores (n = 5) using tomograms without denoising. Measurements were performed using ImageJ[28] (version 1.54f) by obtaining intensity profiles with a line width of 15 pixels (Supplementary Figure 7a). Apparent membrane thickness was defined as the distance between the two intensity minima in the profile across each membrane (Supplementary Figure 7b). For each spore, ten measurements were obtained for each of four membrane groups: the IM, the inner and outer membrane layers of double-layered SCMs, and single-layered SCMs. The ten measurements for each membrane group were

averaged within each spore, yielding one mean value per membrane group per spore.

Differences in membrane thickness among the four groups were primarily evaluated using one-way repeated-measures analysis of variance (ANOVA), with membrane group as the within-spore factor and spore identity as the repeated-measures unit. The Greenhouse–Geisser correction was applied, and pairwise comparisons were performed with Tukey adjustment for multiple testing.

As complementary analyses, linear mixed-effects models were fitted to the individual membrane thickness measurements, with membrane group as a fixed effect. An initial model included spore identity as a random intercept to account for repeated measurements within individual spores. A second model included the spore-by-membrane-group combination as a random intercept to account for clustering of measurements within each membrane group in each spore. Both models were fitted using restricted maximum likelihood estimation. The significance of the fixed effect was evaluated using the Kenward–Roger approximation for degrees of freedom, followed by Tukey-adjusted pairwise comparisons. Statistical analyses were performed using R version 4.6.1 (R Foundation for Statistical Computing), with the afex (version 1.5.1), lme4 (version 2.1.0), lmerTest (version 3.2.1), and emmeans (version 2.0.4) packages. A P value of less than 0.05 was considered statistically significant. Data are presented as mean ± standard deviation (SD), calculated from the mean membrane thicknesses of five spores.

Cryo-ultramicrotomy and cryo-TEM imaging of sections

To preserve the native morphology of the extracellular matrix and enable observation of spore-associated structures, ultrathin sectioning was performed using cryo-ultramicrotomy. A custom-designed cryosphere was implemented to maintain a stable low-temperature and low-humidity environment within the chamber during sectioning. Samples were mounted onto specimen pins and frozen using two different procedures: slow freezing in liquid nitrogen or rapid freezing in liquid ethane. Both types of frozen samples were subsequently subjected to cryo-ultramicrotomy under the same sectioning conditions. After equilibration of the chamber to −80 °C, trimming was performed using a diamond knife (trim20, DiATOME). Electrostatic control was applied during trimming to reduce adhesion of sections to the knife edge. An initial trimming step was conducted with a feed of 1000 nm and a cutting speed of 2.0 mm/s to expose an approximately 100 μm × 100 μm sample surface. Ultrathin sections were subsequently generated with a feed of 80–100 nm and a cutting speed of 1.0 mm/s. Sections were collected onto glow-discharged holey carbon grids using electrostatic attraction to facilitate section transfer. The grids were stored under liquid nitrogen until imaging. For cryo-TEM observation, grids were first screened by low-magnification tiled imaging to identify regions containing sections. High-resolution imaging was performed at 15,000× magnification with a defocus value of −3 μm. Energy-filtered images were recorded with a total exposure time of 2 s, fractionated into 10 frames, at a dose rate of 2.198 $e^{-}/Å^{2}/s$.

Acknowledgements

We thank Saori Maki-Yonekura, Satoshi Katsube and Rie Uno at RIKEN SPring-8 for help in setting up the cryo-FIB-SEM. This work was partially supported by a research grant from the Koyanagi Foundation (TH), JSPS KAKENHI Grant Number 25K09521 (TH), Research Support Project for Life Science and Drug Discovery (Basis for Supporting Innovative Drug Discovery and Life Science Research (BINDS)) from AMED under Grant No. JP25ama121006 (KY), and JST-Mirai Program Grant Number JPMJMI23G2 (KY). We acknowledge the support of the Advanced Imaging and Modeling Center for Soft materials (AIMcS), Tohoku University.

Author Contributions

T.H. and K.Y. conceived and designed the study. R.N., T.T., K.K. and T.H. prepared the samples using cryo-FIB-SEM and cryo-ultramicrotomy. R.N., D.U. and T.H. performed the cryo-electron microscopy experiments. R.N., T.T. and T.H. processed and analyzed the cryo-EM data, interpreted the results and prepared the figures. T.H. wrote the original manuscript. All authors reviewed and edited the manuscript.

Competing interests

The authors declare that they have no conflict of interest.

Supplemental Materials

Supplementary Figures 1-7

Supplementary Tables 1-2

Supplementary Movies 1-8

Data availability

The data supporting the findings of this study are available from the corresponding authors upon reasonable request.

Code availability

No custom software was developed specifically for this study. The image processing and analysis software used in this study is described in the Materials and Methods section.

References

1. Setlow, P. & Christie, G. New Thoughts on an Old Topic: Secrets of Bacterial Spore Resistance Slowly Being Revealed. *Microbiol. Mol. Biol. Rev.* **87**, (2023).

2. Lenz, C. A. & Vogel, R. F. Effect of sporulation medium and its divalent cation content on the heat and high pressure resistance of *Clostridium botulinum* type E spores. *Food Microbiol.* **44**, 156–167 (2014).

3. Ito, Y., Tanaka, T., Ohmachi, T. & Asada, Y. Glutamic Acid Independent Production of Poly(γ-glutamic acid) by *Bacillus subtilis* TAM-4. *Biosci. Biotechnol. Biochem.* **60**, 1239–1242 (1996).

4. Ashiuchi, M. & Misono, H. Biochemistry and molecular genetics of poly-γ-glutamate synthesis. *Appl. Microbiol. Biotechnol.* **59**, 9–14 (2002).

5. Shih, I. L. & Van, Y. T. The production of poly-(γ-glutamic acid) from microorganisms and its various applications. *Bioresour. Technol.* **79**, 207–225 (2001).

6. Flemming, H. C. & Wingender, J. The biofilm matrix. *Nature Reviews Microbiology 2010 8:9* **8**, 623–633 (2010).

7. Flemming, H. C. *et al.* The biofilm matrix: multitasking in a shared space. *Nature Reviews Microbiology 2022 21:2* **21**, 70–86 (2022).

8. Kawata, T., Inoue, T. & Takagi, A. ELECTRON MICROSCOPY OF SPORE FORMATION AND GERMINATION IN *BACILLUS SUBTILIS*. *Jpn. J. Microbiol.* **7**, 23–41 (1963).

9. Laue, M., Niederwöhrmeier, B. & Bannert, N. Rapid diagnostic thin section electron microscopy of bacterial endospores. *J. Microbiol. Methods* **70**, 45 (2007).

10. Dittmann, C., Han, H. M., Grabenbauer, M. & Laue, M. Dormant *Bacillus* spores protect their DNA in crystalline nucleoids against environmental stress. *J. Struct. Biol.* **191**, 156–164 (2015).

11. Mckenney, P. T., Driks, A. & Eichenberger, P. The *Bacillus subtilis* endospore: assembly and functions of the multilayered coat. *Nat. Rev. Microbiol.* **11**, 33 (2012).

12. Bauda, E. *et al.* Ultrastructure of macromolecular assemblies contributing to bacterial spore resistance revealed by in situ cryo-electron tomography. *Nature Communications 2024 15:1* **15**, 1376- (2024).

13. Chua, E. Y. D. *et al.* Better, Faster, Cheaper: Recent Advances in Cryo–Electron Microscopy. *Annu. Rev. Biochem.* **91**, 1 (2022).

14. Klumpe, S. & Plitzko, J. M. Cryo-focused ion beam milling for cryo-electron tomography: Shaping the future of in situ structural biology. *Curr. Opin. Struct. Biol.* **94**, 103138 (2025).

15. Khanna, K. *et al.* The molecular architecture of engulfment during *Bacillus subtilis* sporulation. *Elife* **8**, e45257 (2019).

16. Lam, V. & Villa, E. Practical approaches for cryo-FIB milling and applications for cellular cryo-electron tomography. *Methods Mol. Biol.* **2215**, 49 (2021).

17. Mastronarde, D. N. Automated electron microscope tomography using robust prediction of specimen movements. *J. Struct. Biol.* **152**, 36–51 (2005).

18. Mastronarde, D. N. & Held, S. R. Automated tilt series alignment and tomographic reconstruction in IMOD. *J. Struct. Biol.* **197**, 102–113 (2017).

19. Xu, A. & Xu, C. FastTomo: A SerialEM Script for Collecting Electron Tomography Data. *bioRxiv* 2021.03.16.435675 (2021) doi:10.1101/2021.03.16.435675.

20. Burt, A. *et al.* An image processing pipeline for electron cryo-tomography in RELION-5. *FEBS Open Bio* **14**, 1788 (2024).

21. Tegunov, D. & Cramer, P. Real-time cryo-electron microscopy data preprocessing with Warp. *Nature Methods 2019 16:11* **16**, 1146–1152 (2019).

22. Tegunov, D., Xue, L., Dienemann, C., Cramer, P. & Mahamid, J. Multi-particle cryo-EM refinement with M visualizes ribosome-antibiotic complex at 3.5 Å in cells. *Nature Methods 2021 18:2* **18**, 186–193 (2021).

23. Zheng, S. *et al.* AreTomo: An integrated software package for automated marker-free, motion-corrected cryo-electron tomographic alignment and reconstruction. *J. Struct. Biol. X* **6**, 100068 (2022).

24. Chaillet, M. L., Loenhout, J. van, Leung, M. R., Burt, A. & Tegunov, D. MissAlignment Teaches Itself Better Cryo-ET Tilt-Series Alignment by Making It Worse. *bioRxiv* 2026.04.29.721716 (2026) doi:10.64898/2026.04.29.721716.

25. Liu, Y.-T. *et al.* IsoNet2 determines cellular structures at submolecular resolution without

averaging. *bioRxiv* 2025.12.09.693325 (2025) doi:10.64898/2025.12.09.693325.

26. Last, M. G. F., Abendstein, L., Voortman, L. M. & Sharp, T. H. Streamlining segmentation of cryo-electron tomography datasets with Ais. *Elife* **13**, (2024).

27. Pettersen, E. F. *et al.* UCSF ChimeraX: Structure visualization for researchers, educators, and developers. *Protein Science* **30**, 70–82 (2021).

28. Schneider, C. A., Rasband, W. S. & Eliceiri, K. W. NIH Image to ImageJ: 25 years of image analysis. *Nature Methods 2012 9:7* **9**, 671–675 (2012).

Figure Legends

Figure 1. Schematic illustration of polymer-supported grid preparation for cryo-FIB analysis of natto filaments.

Top: Conventional preparation of cultured cells on a holey carbon grid. Middle: Direct application of natto filaments onto a holey carbon grid. Bottom: Polymer-supported preparation developed in this study, in which a thin polymer film spanning the grid provides continuous support for the natto filaments and improves sample attachment and mechanical stability during cryo-FIB milling. Cross-sectional views on the right illustrate the corresponding sample–support configurations.

Figure 2. Optimization of polymer supports for high-quality cryo-FIB–SEM milling.

The cumulative electron dose for each polymer film is indicated in the upper left corner of each panel. Top: initial images prior to observable damage. Middle: images showing the onset of bubble formation induced by electron irradiation. Bottom: images acquired after further irradiation. In γ-PGA-coated grids, bubble formation is indicated by red arrowheads and is localized near the hole edges, whereas in PAA-coated grids, bubble-like features indicated by a white arrowhead are observed across the entire field of view. Crosses indicate the carbon support film.

Figure 3. Spores and extracellular matrix in cryo-FIB lamellae.

(a) Low-magnification cryo-TEM image of a representative cryo-FIB lamella prepared using a γ-PGA-supported grid, demonstrating the improved preservation and structural integrity achieved by polymer-supported lamella preparation. (b) Cryo-TEM image of spores within a lamella acquired at a nominal magnification of 12,000× (4.796 Å/pixel). White arrowhead indicates frost contamination attached to the lamella surface. Horizontal bright bands observed in the image suggest minor curtaining artifacts introduced during FIB milling. (c) Schematic representation of the multilayered spore structure. From the inside outward: core (white), sub-core membrane (orange), inner membrane (pink), cortex (light green), inner coat (green), and outer coat (purple).

Figure 4. Two-dimensional characterization of sub-core membranes and multilayered spore architecture by cryo-TEM.

(a) High-magnification cryo-TEM image of a mature spore within a cryo-FIB lamella, showing sub-core membranes (SCMs), inner membrane (IM), cortex, inner coat (IC), outer coat (OC), and putative outer membrane. (b-g) Enlarged views of the regions outlined by white boxes in (a). (b) A single-bilayer SCM located beneath an invagination of the IM. (c) An SCM exhibiting a partially double-layered configuration. (d) A double-layered SCM appearing spatially separated from the IM. (e) Multilayered organization of the IC surrounding the cortex. (f) OC at the outermost region of the spore coat. (g) Putative outer membrane, potentially associated with the spore crust or remnants of

the outer forespore membrane.

Figure 5. Three-dimensional distribution of SCMs within a mature bacterial spore.

(a) Zero-degree tilt TEM image of a mature bacterial spore. (b-d) Representative tomographic slices at three different depths within the same reconstructed spore, showing the spatial distribution and morphological diversity of SCMs. (b) Upper, (c) middle, and (d) lower sections of the tomogram. (e) Three-dimensional rendering of segmented membrane structures, showing the inner membrane (pink), single-layered SCMs (yellow), and double-layered SCMs (orange).

Figure 6. Three-dimensional structural characterization of sub-core membranes and spore envelope architecture by cryo-electron tomography.

(a) Representative tomographic slices at two different depths within the same reconstructed mature spore. The left and right panels show different sections of the same tomogram. Boxes indicate the regions enlarged in (b–g). (b–d) Enlarged views of IM invaginations and associated vesicle-like structures at different depths, with the corresponding denoised images (middle row) and three-dimensional renderings (bottom row). Segmentation of the IM invaginations and associated vesicle-like structures was performed using IsoNet2-denoised tomograms. The IM and associated membranes are shown in pink, vesicle-like structures in cyan, and double-layered membrane-like

features in orange. (e) Enlarged view showing single-layered and double-layered SCMs near the IM. (f and g) Enlarged views of a membrane-like structure outside the OC, potentially associated with the spore crust or remnants of the outer forespore membrane.

Figure 7. Large-scale visualization of spores and extracellular environment by cryo-ultramicrotomy.

(a–d) Samples prepared by slow freezing in liquid nitrogen. (e–g) Samples prepared by rapid freezing in liquid ethane. (a, e) Low-magnification overview images of ultrathin sections. (b, f, g) Higher-magnification views of sections containing spores and surrounding regions. Two arrowheads indicate layered structures adjacent to the spore. (c, d) Fourier transforms of the regions indicated by the solid and dashed boxes in (b), respectively, corresponding to crystalline and amorphous regions. Open circles, crosses, triangles, and squares indicate the grid metal frame, the carbon support film, frost contamination introduced after ultrathin sectioning, and spores, respectively.

Figure 8. Proposed models for the formation of double-layered SCMs.

Schematic illustrations of two hypothetical pathways for double-layered SCM formation through invagination and fusion of the IM. Left: Single-invagination fusion model. A single invagination of the IM expands laterally and comes into contact with the original IM. Subsequent membrane fusion

generates an internal vesicle. Right: Multiple-invagination fusion model. Multiple invaginations occur at adjacent sites of the IM and subsequently fuse with one another, generating internal vesicles. In both models, the newly formed vesicles may subsequently fuse to form the inner SCM, while the surrounding invaginated IM forms the outer SCM, resulting in a double-layered SCM. These models are proposed based on the membrane configurations observed by cryo-TEM and cryo-electron tomography and do not represent experimentally established formation pathways.

Figure 1. Schematic illustration of polymer-supported grid preparation for cryo-FIB analysis of natto filaments.

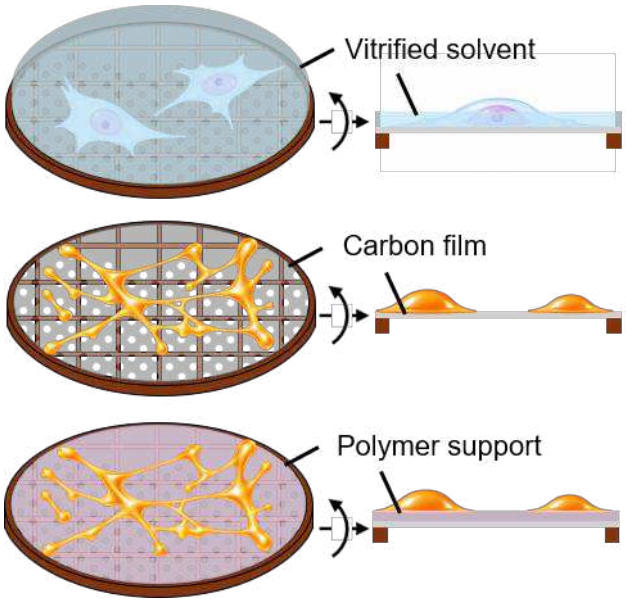


Figure 2. Optimization of polymer supports for high-quality cryo-FIB–SEM milling.

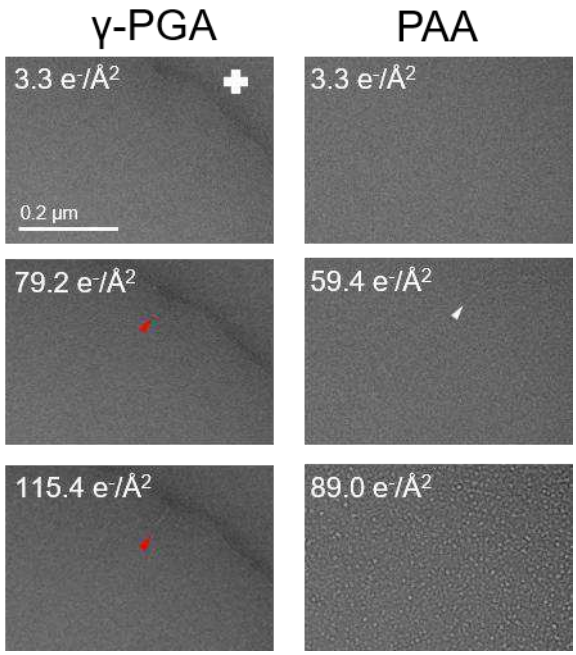


Figure 3. Spores and extracellular matrix in cryo-FIB lamellae.

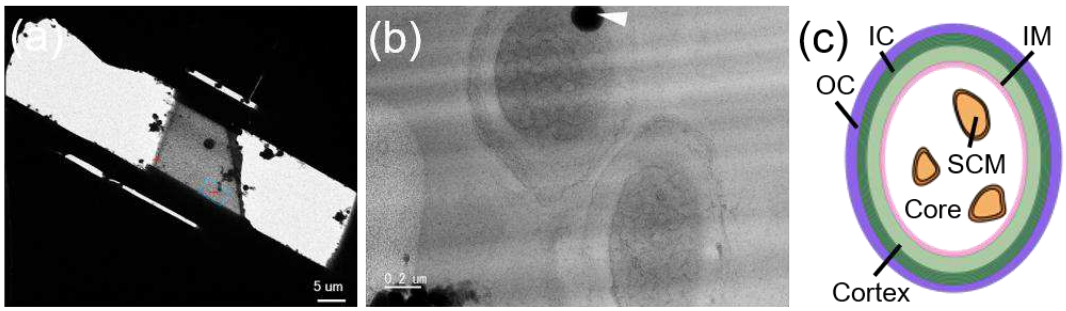


Figure 4. Two-dimensional characterization of sub-core membranes and multilayered spore architecture by cryo-TEM.

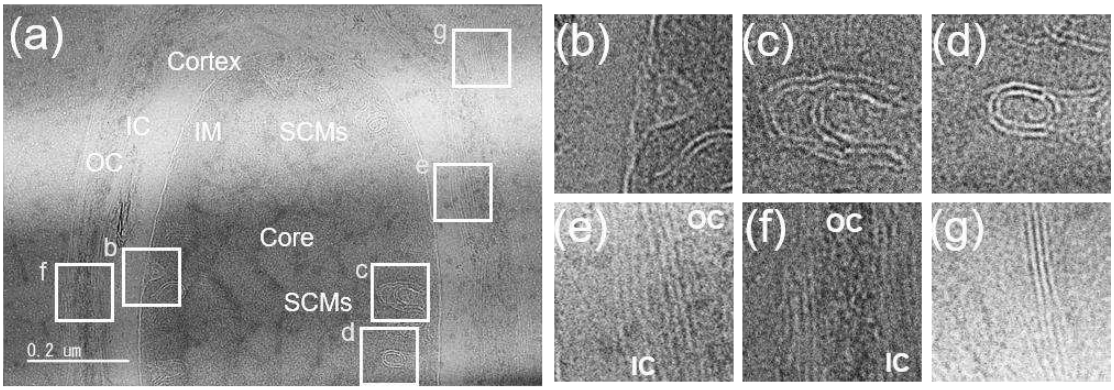


Figure 5. Three-dimensional distribution of SCMs within a mature bacterial spore.

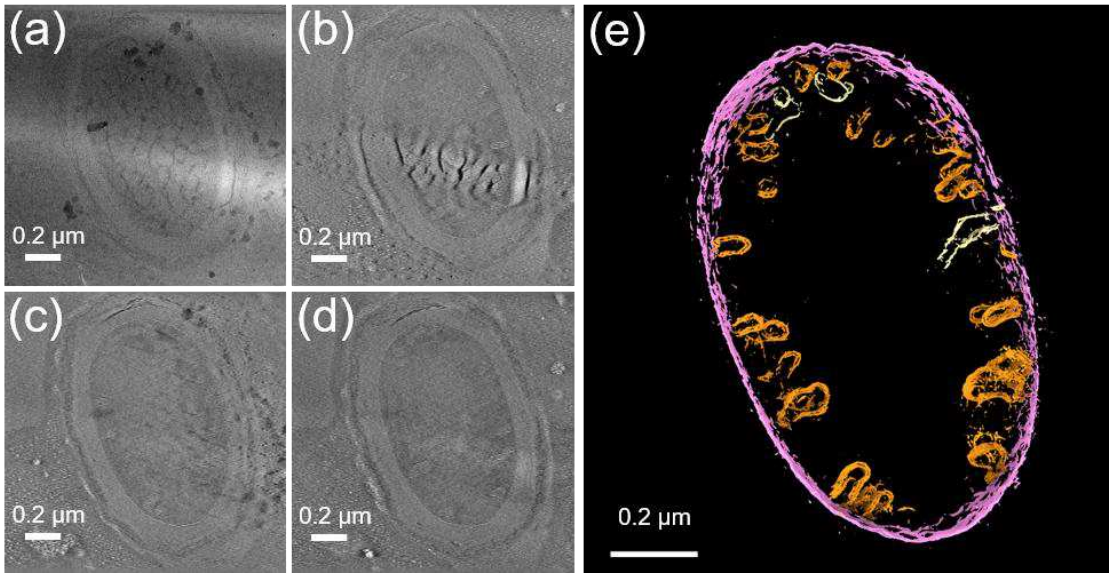


Figure 6. Three-dimensional structural characterization of sub-core membranes and spore envelope architecture by cryo-electron tomography.

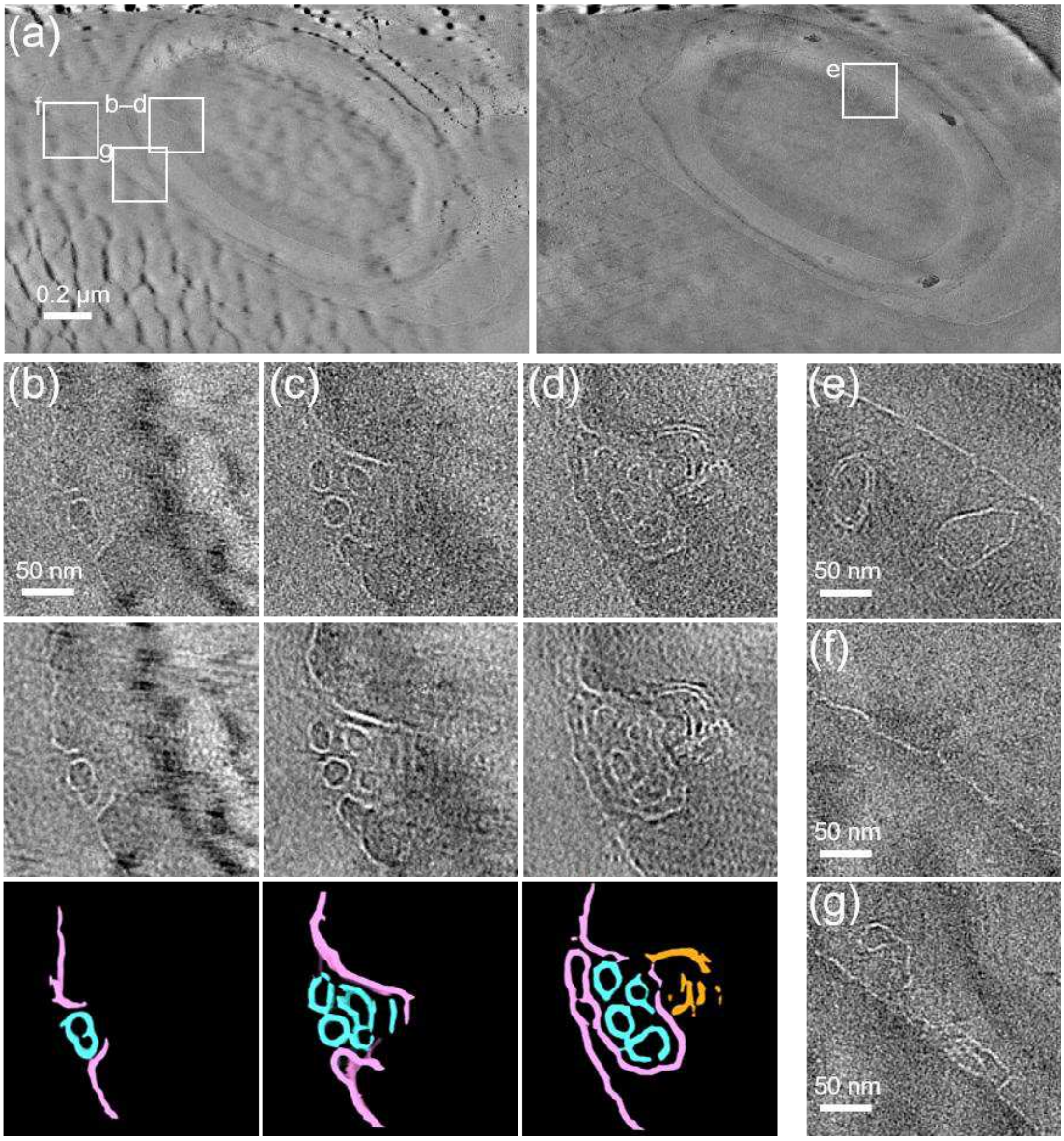


Figure 7. Large-scale visualization of spores and extracellular environment by cryo-ultramicrotomy.

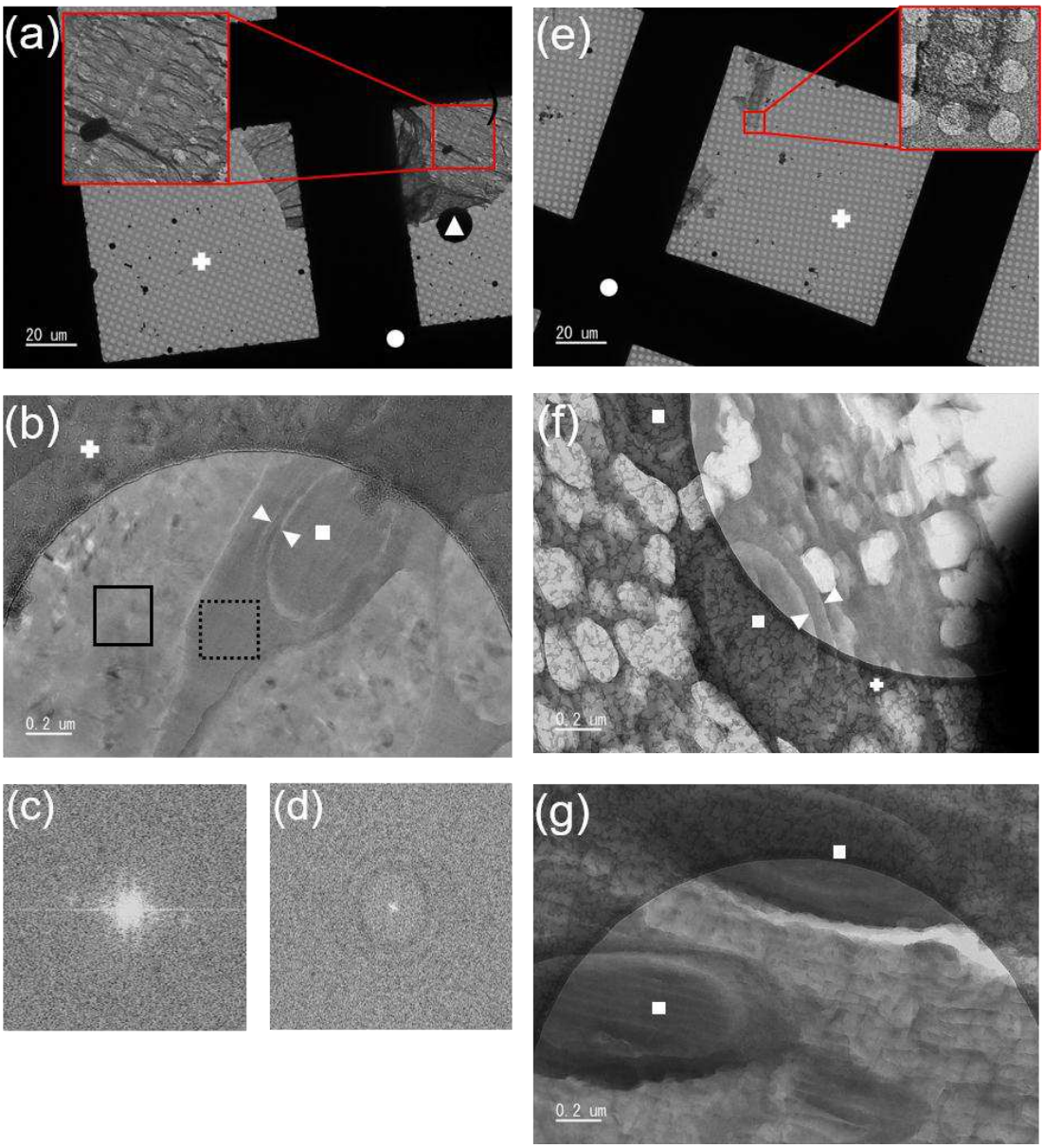
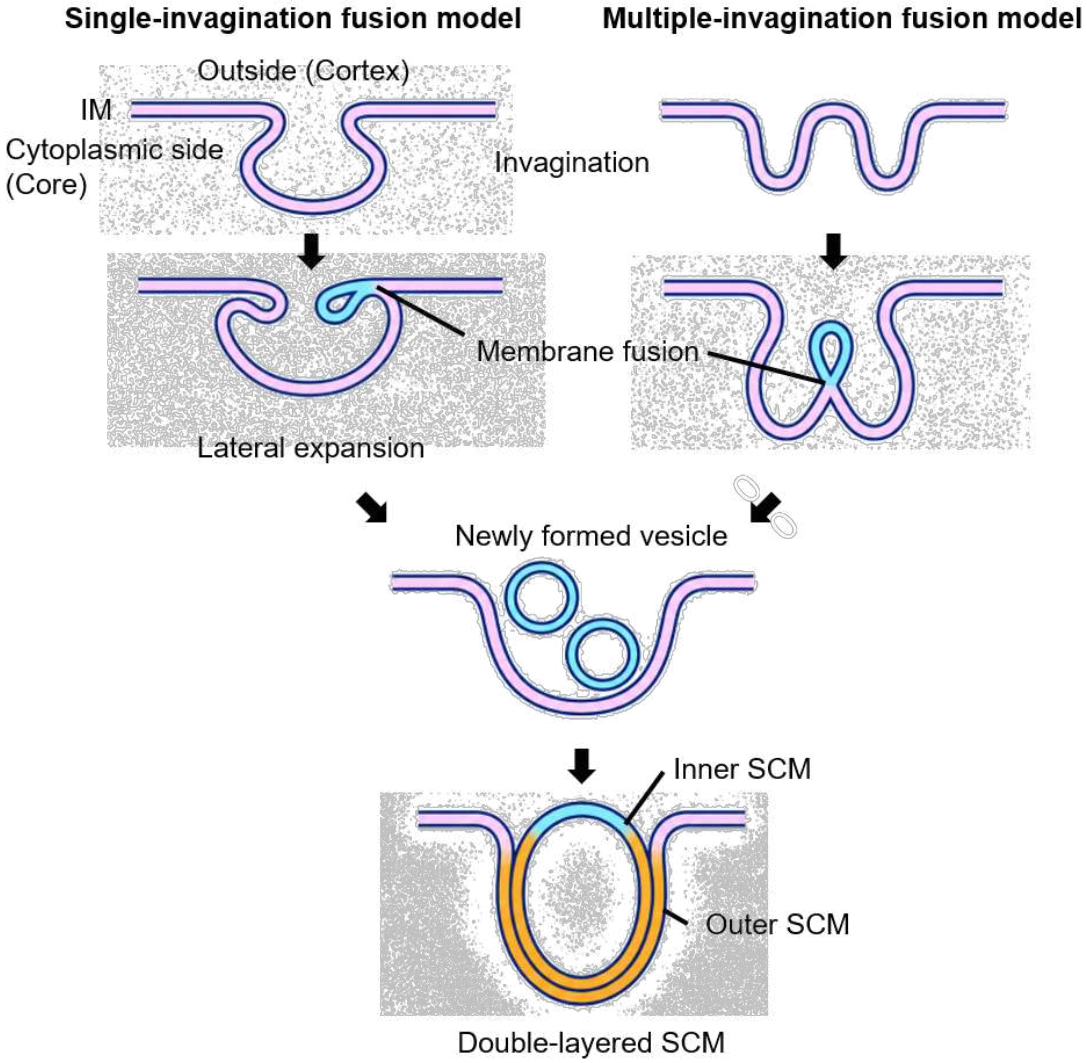


Figure 8. Proposed models for the formation of double-layered SCMs.



Supplementary Files

This is a list of supplementary files associated with this preprint. Click to download.

- SupplementaryInformationv1.docx
- MovieS8.avi
- MovieS7.avi
- MovieS1.mp4
- MovieS4.avi
- MovieS5.avi
- MovieS3.avi
- MovieS2.avi
- MovieS6.mp4